Nucleic Acids Research, 2025, **53**, gkaf148
https://doi.org/10.1093/nar/gkaf148
Molecular and Structural Biology

Conformational reorganization and phase separation drive hyper-editing of ADR-2–ADBP-1 complex

Jianqiang Mu[1,2,†], Cang Wu[1,3,†], Kaiming Xu[4], Xingang Liu[1,2], Yajuan Fu[1,2], Zhen Zhang[1,2], Jingwei Yu[3], Chenyang Xue[1,2], Zi Wang[4], Xinmeng Chen[1,2], Yanhong Chen[3], Guangshuo Ou[4,*], Zhongmin Liu[1,2,5,*]

[1]Shenzhen Key Laboratory of Biomolecular Assembling and Regulation, School of Life Sciences, Southern University of Science and Technology Shenzhen, 518055 Guangdong, China
[2]Department of Immunology and Microbiology, School of Life Sciences, Southern University of Science and Technology, Shenzhen 518055 Guangdong, China
[3]Department of Biology, School of Life Sciences, Southern University of Science and Technology, Shenzhen 518055 Guangdong, China
[4]Tsinghua-Peking Center for Life Sciences, Beijing Frontier Research Center for Biological Structure, School of Life Sciences and MOE Key Laboratory for Protein Science, Tsinghua University, Beijing 100084, China
[5]Institute for Biological Electron Microscopy, Southern University of Science and Technology, Shenzhen 518055 Guangdong, China

[*]To whom correspondence should be addressed. Email: liuzm@sustech.edu.cn
Correspondence may also be addressed to Guangshuo Ou. Email: guangshuoou@mail.tsinghua.edu.cn
[†]These authors contributed equally to this work as first authors.

Abstract

Adenosine deaminase acting on RNA (ADAR) proteins, which mediate adenosine-to-inosine editing of double-stranded ribonucleic acid (dsRNA) substrates, play essential roles in balancing innate immunity. Using cryogenic electron microscopy, we solved the structure of the *Caenorhabditis elegans* ADR-2–ADBP-1 complex (stoichiometric ratio, 2:2), which is an asymmetric ADR-2 dimer with one editing site blocked by the other ADR-2. Unexpectedly, dsRNA recruitment triggered dissociation of the ADR-2 dimer, exposing more competent dsRNA editing sites. Furthermore, high dsRNA and protein concentrations caused the formation of liquid–liquid phase-separated puncta, in which significantly greater editing activity was observed, indicating that organizational transitions enable the ADR-2–ADBP-1 complex to perform dsRNA hyper-editing. Our findings suggest that the ADAR editing mechanism adapts to different conditions via conformational reorganization.

Graphical abstract

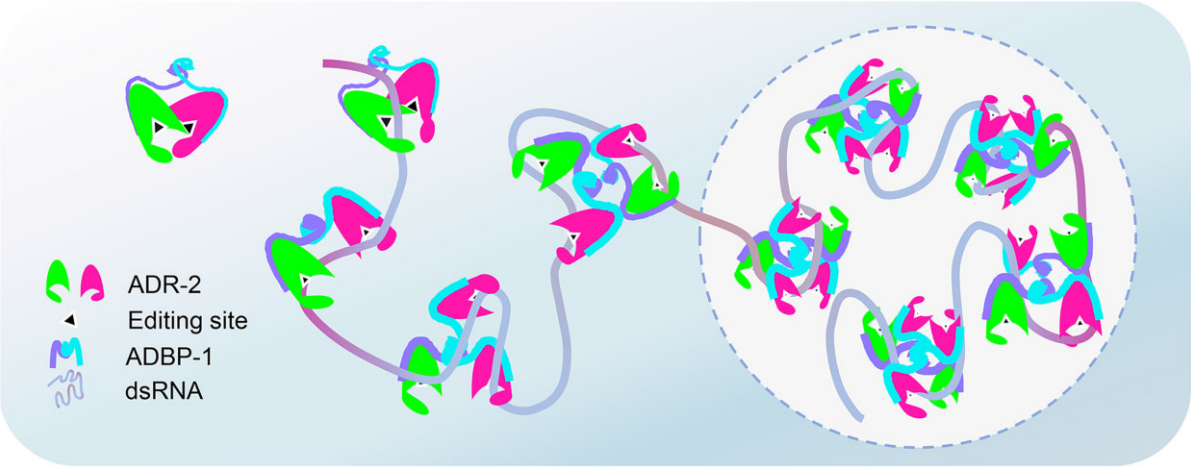

Introduction

The ribonucleic acid (RNA) editing process of adenosine-to-inosine (A-to-I) conversion, mediated by adenosine deaminase acting on RNA (ADAR) enzymes, plays an essential role in metazoan biological processes, particularly innate immunity [1–4]. A-to-I editing yields inosine, which preferentially base

Received: August 5, 2024. **Revised:** February 6, 2025. **Editorial Decision:** February 11, 2025. **Accepted:** February 17, 2025

pairs with cytosine (Fig. 1A), thereby influencing the destiny of messenger RNAs (mRNAs)—by editing their coding regions, introns, and 3′ untranslated regions—and the homeostasis of noncoding RNAs [5].

The *Caenorhabditis elegans* genome encodes ADR-1 and ADR-2, of which ADR-2 is essentially orthologous to human (h)ADAR1 [6]. Notably, although the deletion of *hADAR1* causes embryonic death, the loss of ADARs in *C. elegans* leads to reduced chemotaxis [7]. ADR-2 is the exclusive active RNA deaminase in *C. elegans*, primarily targeting noncoding sequences [8, 9]. The ADAR family is involved in antiviral responses [10], and recent studies suggest the loss of *adr-1* or *adr-2* increases susceptibility to *Pseudomonas aeruginosa* [11]. ADARs also regulate normal behavior and lifespan in *C. elegans* [8]. Recently, we discovered that *C. elegans* expressing a constitutively active mitogen-activated protein kinase, DYF-5 (referred to as DYF-5CA), exhibits disrupted sensory cilia. This disruption is caused by ADR-2-mediated hyper-editing of *dyf-5CA* pre-mRNA, which impairs *dyf-5CA* mRNA splicing and blocks the translation of DYF-5CA. Interestingly, mutations in the RNA adenosine deaminase ADR-2, but not ADR-1, were able to rescue the ciliary defects caused by DYF-5 [12]. Notably, ADAR-mediated hyper-editing is not limited to *C. elegans*; it has also been widely observed in various species, including humans, mice, rats, frogs, and flies [13]. However, the precise mechanism by which ADAR efficiently performs hyper-editing on double-stranded ribonucleic acid (dsRNA) remains unclear.

The A-to-I editing activity of ADARs is reportedly dependent on dimerization [14–16]. However, crystallized hADAR2–RNA complexes revealed that hADAR2 can capture dsRNA in monomeric or dimeric states [17, 18], indicating diverse ADAR editing modes may exist in distinct physiological contexts. All current structural information is derived from truncated hADAR2 and chemically modified dsRNA [17–19], which limits its power to uncover the mechanism of ADAR editing, particularly as hyper-editing may occur simultaneously at multiple sites within an RNA sequence.

Unlike hADAR1 and hADAR2, ADR-2 forms a stable complex with partner protein ADR-2 binding protein 1 (ADBP-1), homologs of which have not been identified in other species [20]. ADR-2 is mainly found in the nucleus, governed by ADBP-1 [21, 22]. Wilkins *et al.* reported that A-to-I editing was absent in *ADBP-1* mutants, highlighting the essential role of ADBP-1 for ADR-2 deaminase activity [20]. However, the cytoplasmic-localized ADR-2 may harbor functions independent of ADBP-1, such as antagonizing the RNA interference pathway in *C. elegans* [20], which is similar to the roles of ADAR proteins in mammals [23] and *Drosophila* [24]. Thus, it remains to be determined whether ADBP-1 is necessary for ADR-2's editing activity, and further research is needed to understand the regulatory mechanism of ADBP-1 on ADR-2, particularly due to the lack of a solved structure of the ADR-2–ADBP-1 complex.

Accumulating evidence suggests that liquid–liquid phase separation (LLPS) plays a crucial role in regulating the homeostasis and activity of ribonucleoprotein complexes, particularly the nonmembrane organelles known as stress granules [25–27]. The P150 isoform of hADAR1 localizes to and negatively regulates the formation of stress granules via its RNA editing-independent activity [28]. Interestingly, coimmunostaining of immature cortical neurons revealed that nuclear hADAR2 could localize to nucleoli, where multiphase liquid condensates were observed [29, 30]. Moreover, our data suggested that ADR-2 and ADBP-1 exhibit a punctate distribution in *C. elegans*. Recent studies have revealed that the targeted recruitment of pre-mRNAs to liquid phase-separated nuclear speckles can enhance mRNA splicing [31], indicating that LLPS may have widespread regulatory roles in RNA processing. However, the mechanism underlying LLPS regulation of ADAR activity remains elusive.

Using cryogenic electron microscopy, we determined the high-resolution structure of the *C. elegans* ADR-2–ADBP-1 complex, which adopts a heterotetrameric organization. Moreover, we found that the recruitment of dsRNA by the dsRNA-binding domain (dsRBD) could dissociate the ADR-2 dimer, yielding a liquid condensate in which ADR-2 hyper-edits dsRNA substrates, which may represent the general hyper-editing mode of ADAR proteins.

Materials and methods

Cloning, expression, and purification

The full-length complementary DNA (cDNA) of *ADR-2* (NM_066193.4) and *ADBP-1* (NM_064038.7) was subcloned into the pCAG vector with C-terminus tandem twin Strep-tag and 3 × Flag tag by homologous recombination (Vazyme, C112-01), respectively. Its point mutants were generated with the Fast Mutagenesis System kit (Transgen, FM111), and the coding region of the gene was verified by Sanger DNA sequencing (Tsingke, Guangzhou).

The *C. elegans* ADR-2 was expressed through transient transfection of ADR-2 plasmids into human embryonic kidney cells (HEK293F) using polyethylenimine (PEI) (YEASEN, 40816ES03) as the transfection reagent. Transfections were performed at a cell density ranging from 2.0 × 10^6 cells/ml to 2.5 × 10^6 cells/ml. Plasmid DNA was mixed with PEI in a ratio of 1:2 (w:w) and incubated in a serum-free medium for 20 min at room temperature (RT) before being added to the cell culture. After 48 h post-transfection, cells were harvested by centrifugation (800 *g*, 10 min, 4°C), flash-frozen in liquid nitrogen, and stored at −80°C until further use.

For purification, cells were thawed and gently resuspended in lysis buffer for 0.5 h containing 50 mM Tris–HCl (pH 7.9), 200 mM KCl, 10% glycerin, 2 mM dithiothreitol (DTT) and 1% Triton X-100 (Sigma–Aldrich) with EDTA-free protease inhibitor cocktail (Roche). All subsequent steps were performed at 4°C. The solubilized fraction was clarified by centrifugation at 51 428 *g* for 1 h to remove insoluble debris. The supernatant was then incubated with Strep-Tactin® Sepharose® (IBA, LifeSciences) for 1.5 h by rotation. After incubate, the resin was collected and washed with wash buffer containing 50 mM Tris–HCl (pH 7.9), 100 mM KCl, 10% glycerin, and 2 mM DTT, followed by protein eluted with wash buffer plus 50 mM biotin. The eluate was concentrated and further purified by anion-exchange with a Mono Q™ 5/50 GL (GE Healthcare) and size-exclusion chromatography (SEC) on a Superose™ 6 Increase 3.2/300 column (GE Healthcare) in a SEC buffer containing 25 mM Tris–HCl (pH 7.9), 100 mM NaCl, 2 mM DTT, and 0.02% Nonidet P 40. Peak fractions were collected and concentrated to ∼0.5–1 mg/ml for cryo-electron microscopy (cryo-EM) analysis. Recombinant mutant proteins were expressed and purified as above.

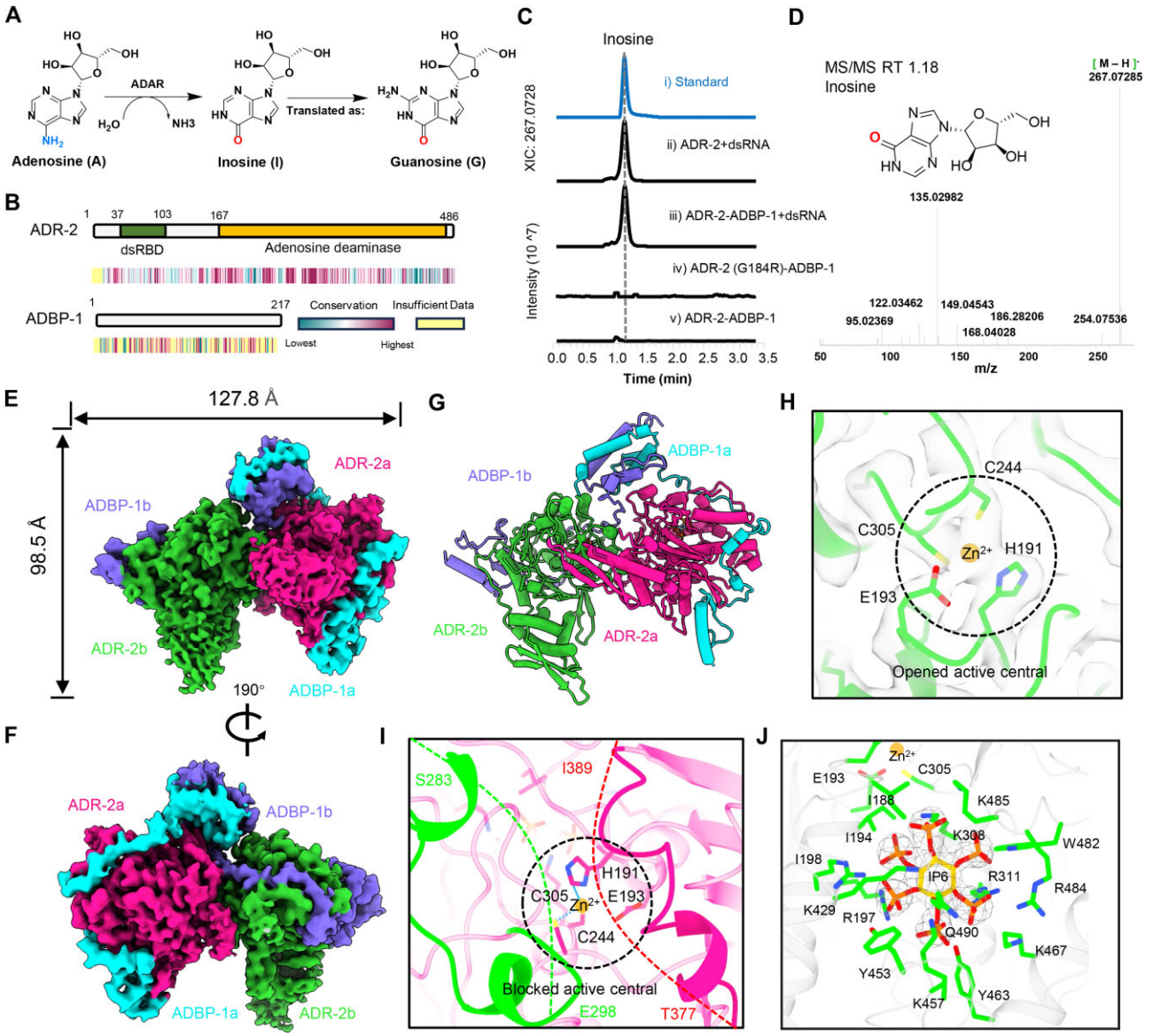

Figure 1. Overall structure of the heterotetrameric ADR-2–ADBP-1 complex. (**A**) ADAR enzyme facilitates a hydrolytic deamination reaction wherein an adenosine (**A**) undergoes the removal of an amine group, leading to its conversion into inosine (**I**), which is read as guanosine (**G**) by polymerase enzymes. (**B**) Schematic diagram showing the domain organizations of ADR-2 and ADBP-1. The heatmap below shows the amino acid sequence conservation of ADR-2 and ADBP-1 proteins, respectively. (**C**) LC-MS/MS analysis of the editing activity of the ADR-2 and ADR-2–ADBP-1 complexes. The *Y*-axis represents counts (reaction abundance), and the *X*-axis represents time. Comparative LC-MS extracted ion chromatograms (EICs, *m*/*z* 267.0728) show the following products: (i) inosine standard (blue curve); (ii) products from the reaction of ADR-2 with the substrate dsRNA; (iii) products from the reaction of the ADR-2–ADBP-1 complex with the substrate dsRNA; (iv) the ADR-2–ADBP-1 complex without the substrate dsRNA. Substrate dsRNA: Synthesized 57 bp sequence from *dyf-5* gene intron 6. (**D**) LC-MS/MS mass spectra of inosine. Experiments were performed in triplicate and repeated three times with similar results. (**E** and **F**) Cryo-EM map of the ADR-2–ADBP-1 tetramer complex in the apo conformation at 3.29 Å resolution (E) and clockwise rotation of 180° (F). (**G**) Ribbon diagram of the ADR-2–ADBP-1 tetramer atomic model in the same orientation as in panel (E). (**H**) Density in the cryo-EM map of an open catalytic active center of ADR-2b. The model of ADR-2b is shown in lime. Residues of H191, C244, C305, and E396 are represented by green sticks, and zinc ions are shown as orange spheres. The active center is marked by a black dotted circle. Blocked catalytic active center of ADR-2a. The amino acid chain S283 to E298 on ADR-2b (dashed green line) and the amino acid chain T377 to I389 on ADR-2a (dashed red line) block the accessibility of ADR-2a's active center. (**J**) Representation of the hexakisphosphate (IP6)-binding pocket of ADR-2b. The cryo-EM density for the bound IP6 is shown in gray mesh, and residues contacting IP6 are shown as sticks. The same color scheme is used throughout the manuscript.

The assembly of the ADR-2 and ADBP-1 complex was performed through transient cotransfection of ADR-2 and ADBP-1 plasmids into HEK293F cells. The ADR-2–ADBP-1 complex utilized for cryo-EM grid preparation was purified employing identical procedures as those used for purifying ADR-2.

Electron microscopy sample preparation and data collection

ADR-2–ADBP-1 complex (3 μl) at a concentration of 1 mg/ml was applied to glow-discharged (75 s at 15 mA) 300-mesh Quantifoil R 1.2/1.3 grids, and subsequently blotted 4 s and waited for 10 s using a Vitrobot Mark IV (Thermo Fischer Scientific) at 4°C and 100% humidity, and then frozen in liquid ethane. The grids were imaged on a Thermo Fisher Krios G3i microscope (Thermo Fisher Scientific), equipped with a GIF Quantum energy filter (Gatan) and K3 Summit detector (Gatan). The energy filter was operated with a slit width of 20 eV to remove inelastically scattered electrons. Image stacks were collected using EPU2 software at a pixel size of 0.855 Å/pixel or 0.856 Å/pixel with a total dose of 50 $e^{-}/Å^{2}$ and a defocus range of −1.0 to −2.0 μm. One stack contains 32 frames.

Cryo-EM data processing, model building, and refinement

The collected data were processed using the cryoSPARC (v4.0) [32]. Movies of the single datasets were motion-corrected using Patch Motion Correction and contrast transfer function (CTF) was estimated with Patch CTF estimation in cryoSPARC. Two thousand images were used to generate an initial particle-set by blob picker in cryoSPARC. Particles were binned to a pixel size of 1.71 Å, and extracted with a box size of 144 pixels. Two-dimensional (2D) classification was performed in cryoSPARC. High-quality 2D class averages representing projections in different orientations were selected as templates for Topaz [33] training of the entire dataset. The particles were then subjected to heterogeneous refinement in cryoSPARC, and then 2D classification in cryoSPARC to remove most of the bad particles. The selected particles were used to generate the final map by using nonuniform refinement with an estimated average resolution of 3.29 Å using the gold standard FSC (FSC = 0.143).

As a starting point, the model predicted by AlphaFold2 was manually docked to the map using UCSF ChimeraX [34] (version 1.4). The presented model was manually refined using COOT [35] (version 0.9.8) and automatically refined with the Phenix Real-space refinement tool [36] (Phenix v1.20.1). The statistics of the 3D reconstruction and model refinement are summarized in Supplementary Table S1.

Protein crosslinking analysis

For the glutaraldehyde (GA) treatment, reaction mixtures containing 50–100 μg of interacting proteins in 20 mM HEPES buffer (pH 7.5) in a total volume of 100 μl were treated with 5 μl of a freshly prepared 2.3% GA solution. The treatment was conducted for 2 to 5 min at 37°C. The reaction is terminated by the addition of 10 μl of 1 M Tris–HCl, pH 8.0. The cross-linked samples were analyzed using SDS–PAGE.

Label-free thermal shift assay

Label-free thermal assays were conducted in accordance with the Tycho NT.6 System Operation Manual (NanoTemper Technologies). Briefly, prior to sample loading, protein samples of ADR-2 and ADR-2–ADBP-1 complex underwent centrifugation at 16 000 *g* for 15 min at 4°C in SEC buffer. Following this, the samples were introduced into single-use Tycho NT.6 capillaries. All measurements adhered to the Tycho NT.6 system's default procedure, ramping the temperature from 35 to 95°C at a rate of 30°C/min. The inflection point temperature (T_i) was derived by plotting the unfolding curve correlating the brightness ratio of 350 nm/330 nm against the sample temperature, calculated automatically by the Tycho NT.6 software. Raw data files were exported for plotting unfolding curves, and the data were presented as the mean ± standard deviation (SD) of three independent experiments using GraphPad Prism version 9.0.0.

In vitro assay of ADR-2 editing-activity assay

In the editing activity assays, the ADR-2 or ADR-2–ADBP-1 complex was incubated with substrate dsRNA synthesized from the 57 bp sequence of intron 6 of the *dyf-5* gene in a buffer (25 mM Tris, pH 7.9; 100 mM NaCl; 2 mM DTT) at 37°C for 1 h. Following incubation, the reaction was extracted with chloroform and centrifuged at 16 000 g for 30 min. The supernatant was then collected and digested to nucleosides using the Nucleoside Digestion Mix (NEB, M0649S) according to the manufacturer's protocol. The reaction mixture was subjected to two chloroform extractions, after which the aqueous layer was collected and lyophilized. The digested nucleosides were redissolved in 50 μl methanol for LC-MS/MS analysis. Samples were either analyzed immediately or stored at −80°C for later analysis. Inosine 5′-triphosphate trisodium was purchased from Macklin (I812079). The ADR-2 and ADR-2–ADBP-1 complex samples without substrate dsRNA, as well as the standalone substrate dsRNA samples, were directly extracted with chloroform, and all other steps were performed as described above as a negative control.

Liquid chromatography with tandem mass spectrometry (LC-MS/MS) analysis was carried out on a Thermo LC-MS Q.Exactive-Orbitrap system with a Kinetex 1.7 μm EVO C18 (100 mm × 2.1 mm; Phenomenex, USA). Milli-Q (solvent A) and acetonitrile (solvent B, containing 0.1% CHOOH) were used as mobile phases. The flow rate was set at 0.3 ml/min. The injection volume was 10 μl. The solvent gradient was as follows (solvent B%): 4% (0.0–1.0 min), 4%–6% (1.0–3.0 min), 6%–8% (3.0–4.0 min), 8%–50% (4.0–5.5 min), 50%–100% (5.5–6.5 min), 100% (6.5–7.5 min), 100% to 4% (7.5–8.5 min), 4% (8.5–10.0 min). The MS capillary temperature was set to 320°C, with the HESI source and heat block maintained at 370°C. The MS data were acquired in negative modes (source voltage: 4.0 kV, resolution: 70 000, AGC target: 3e6, scan range: 200–700 m/z).

To accurately detect inosine in tested samples, we first used the above-mentioned LC-MS method to analyze the inosine standard. A single peak was observed on the chromatograph at RT (retention time) 1.18 min, with an m/z value of 267.07285 $[M\text{-}H]^{-}$, which matches the calculated value of 268.08. Subsequently, the same peak selection method was applied to assess the tested samples, allowing for a qualitative evaluation of inosine presence. The chromatographic results

are presented on a fixed intensity scale (10^7), along with the MS/MS data obtained from the tested samples.

Blunt-end cloning and sequencing analysis

The chloroform-extracted ADR-2 edited E5I8_RNA product was reverse transcribed *in vitro* using the FastKing cDNA First Strand Synthesis Kit (TianGen, KR116) with the specific primer 5′-GGGATGAATGGCCAG-3′. Subsequently, the reverse transcription PCR (RT-PCR) was performed to amplify the target sequences using primers E5I8-F (TAATACGACTCACTATAGGGCTGAAAATTGAAAGAAATAGAAAGG) and E5I8-R (GATGAATGGCCAGAAGGTTA). The resulting amplified products were purified by gel extraction and then cloned into the pESI-Blunt simple vector (Yeasen, 10910ES20). Positive clones containing inserts were subjected to sequencing analysis to identify nucleotide changes and compared with the original sequence of *dyf-5* gene.

RNase A treatment

The purified ADR-2–ADBP-1 complex and its mutants were treated with RNase A (Sigma, R6513) at a final concentration of 20 μg/ml, followed by incubation at 37°C for 30 min. The treated samples were then subjected to sequential affinity chromatography using a second tag for an additional round of affinity purification. The final samples were used for detection via western blot or SDS–PAGE.

Pull-down assay

To study the interaction between ADR-2 and ADBP-1, we cotransfected HEK293F cells with plasmids encoding either wild-type or mutant Strep-tagged ADR-2 and wild-type or mutant Flag-tagged ADBP-1, using a 1:1 molar ratio. The transfection and protein purification procedures were performed as previously described. We then verified the interaction between ADR-2 and ADBP-1 through western blot analysis of the purified protein products.

Western blotting

Western blotting was performed as previously reported [37] using the following primary antibodies: monoclonal anti-strep (HuaxingBio, HX1988) and monoclonal anti-Flag (HuaxingBio, HX1801). Briefly, the extracts were separated by SDS–PAGE and then samples were transferred to polyvinylidene fluoride (0.45 μm Immobilon, EMD Millipore). Membranes were blocked with 5% nonfat milk for 1 h followed by incubation with a primary antibody overnight at 4°C on a shaker. Then they were washed and incubated with HRP-conjugated goat anti-mouse IgG (H + L) (HuaxingBio, HX2032) at 37°C for 1 h, and then were visualized using a Super ECL Detection Reagent (YEASEN, 36208ES60).

Electrophoretic mobility shift assay

The 5′-fluorescein amidite (FAM)-labeled RNA chains (5′-6-FAM-AAGGAUUACUGUAGUUUUCGC) and unlabeled complementary chains were synthesized by the GenScript Biotech Corp. Prior to use, RNA was heated in metal-free water for 2 min at 90 °C followed by slow cooling to room temperature to induce RNA duplex formation. Electrophoretic mobility shift assays used 2 μl of 200 nM labeled RNA incubated with the desired protein on ice for 30 min in a 20 μl reaction containing 25 mM Tris–HCl (pH 7.9), 100 mM KCl, and 2 mM DTT. The samples were electrophoresed on 6% native-PAGE at 4 °C in running buffer containing 0.5× Tris-glycine buffer under an electric field of 15 V/cm for 70 min, after which the gel was subsequently visualized with a Chemiluminescent Imaging System (Tanon Science & Technology).

Protein fluorescence labeling

The buffer employed for protein purification was substituted with a solution comprising 100 mM $NaHCO_3$ (pH 8.3), 100 mM NaCl, and 2 mM DTT. Alexa Fluor® 488 ester (Thermo Fisher, A20000) was dissolved in dimethyl sulfoxide at a stock concentration of 5 mM. The fluorophore was combined with the corresponding protein solution in a 1:1 ratio following the manual for Alexa Fluor® 488 ester and incubated at room temperature for 1 h. The reaction was terminated by adding 200 mM Tris (pH 8.2). Subsequently, to eliminate unlabeled fluorophores, the labeled proteins underwent exchange into a buffer containing 50 mM Tris (pH 8.2), 100 mM NaCl, and 2 mM DTT, facilitated by a HiTrap desalting column (GE Healthcare). The fluorescence labeling efficiency was quantified using Nanodrop 2000 (Thermo Fisher). In fluorescence imaging experiments, the ultimate molar ratio of fluorescently labeled proteins to unlabelled proteins was maintained at 1:100.

In vitro phase separation assay

In vitro phase separation assay was conducted in a buffer consisting of 50 mM Tris (pH 7.9), 100 mM NaCl, and 2 mM DTT. Droplet assembly for the ADR-2–ADBP-1 complex and the ADR-2–ADBP-1 (ΔdsRBD) complex was initiated by mixing with a final concentration of 4% (w/v) PEG-8000 (Sigma, 25322-68-3). Phase separation of the ADR-2–ADBP-1 complex in the presence of RNA was assessed by adding RNA to the ADR-2–ADBP-1 complex. For fluorescence imaging, proteins were gently mixed by pipetting 3–5 times and then dispensed onto 384-well plates and observed under a Leica TCS SP8 microscope equipped with ×63 water immersion objectives.

Fluorescence recovery after photo-bleaching assay (FRAP)

For the *in vitro* experiments, fluorescence recovery after photo-bleaching assay (FRAP) was carried out with samples in 384-well microscopy plates using a Leica TCS SP8 microscope equipped with ×63 water immersion objectives. A region of a 2–6 μm diameter circular region of interest (ROI) was bleached using a laser intensity of 100% at 488 nm. The recovery from photobleaching was monitored for a total of 220 s after bleaching.

For the *in vivo* experiments, FRAP was carried out at 20°C using Zeiss LSM900 with Airyscan2 confocal microscopy (Carl Zeiss). Condensates in the nuclei of young adult worms were chosen for photobleaching. A 488 nm laser at 100% power was used for photobleaching, and images were acquired every 1.5 s for a total of 15 s after bleaching. The data were normalized to the fluorescence before the bleach.

Worm strains and culture

Wild-type Bristol N2 *Caenorhabditis elegans* laying eggs were cultured on nematode growth medium (NGM) plates seeded

with OP50 *Escherichia coli* cells. Strains were maintained at 20°C unless otherwise noted.

Plasmid micro-injections

For fluorescence tag knockin, homology recombination (HR) templates were constructed by cloning the homology arms into pPD95.77 plasmids using In-Fusion Advantage PCR Cloning Kit (Clontech, #639621). Subsequently, fluorescence tag sequences were inserted into the constructs with a flexible linker before the stop codons or after the start codon ATG. Target sites in the templates were modified with synonymous mutations.

To knockin point mutations, we constructed the mutation sites with synonymous mutations to acquire the specific restriction enzyme recognition sites on the HR templates by In-Fusion Advantage PCR Cloning Kit. All variations were verified by the sanger sequencing of the entire genes, and no other mutations were inserted on the target genes.

Forward genetic screens

We employed forward genetic screening to identify suppressors of *dyf-5CA* [12]. In brief, *dyf-5CA* (cas501) mutant animals (P0) were treated with ethyl methanesulfonate (EMS) during the late L4 stage. Subsequently, they were transferred to standard culture conditions until adulthood. After bleaching the adult animals, eggs (F1) were distributed for culturing. Adult F2 animals were then collected and subjected to dye filling. Dye-positive mutant animals were individually cultured, and their offspring were further validated through dy- filling experiments.

Dye-filling assay

The DiI fluorescence dye-filling assay is commonly used to evaluate ciliary function and integrity. Dye-filling defective animals develop abnormal ciliary structures and exhibit defects in behavioral assays like osmotic avoidance and chemotaxis [13, 38, 39]. The dye-filling assay is performed using the fluorescence dye DiI (DiI 1,1′-dioctadecyl-3,3,3′,3′,tetramethylindo-carbocyanine perchlorate, Sigma) filling assay, as described [12]. Young adult worms were incubated in 100–200 μl of M9 (5.8 g/l Na_2HPO_4, 3.0 g/l KH_2PO4, 0.5 g/l NaCl, and 1.0 g/l NH_4Cl) buffer mixed with dyes at a working concentration of 20 μg/ml for 30 min in darkness at room temperature. Subsequently, worms were then transferred to seeded NGM plates and examined for dye uptake 2 h later using a fluorescence stereoscope or fluorescence compound microscope. A minimum of 50 animals from each strain were observed across three independent assays.

Results

ADR-2 formed a homodimer independent of RNA and ADBP-1

To facilitate our investigation of the ADR-2 editing mechanism, we first expressed and purified the full-length *C. elegans* ADR-2 (~55 kDa) using the HEK293F cell line (Fig. 1B and Supplementary Fig. S1A). Interestingly, pull-down assays revealed that Strep-tagged ADR-2 could be pulled down with Flag tag-fused ADR-2, suggesting ADR-2 formed a dimer or oligomer in the absence of ADBP-1 (Supplementary Fig. S1B and C). Notably, ADR-2 proteins eluted at ~110 kDa by SEC (Supplementary Fig. S1D); moreover, treatment of ADR-2 proteins with the cross-linking reagent GA resulted in the conversion of the monomeric form into a dimeric form of ~110 kDa by SDS–PAGE (Supplementary Fig. S1E and F). Collectively, these data suggest that ADR-2 forms a dimer in its primary state.

To explore whether ADR-2 dimerization depended on RNA substrates, we treated with nuclease during the protein purification process to eliminate potential interference from RNAs. Subsequent pull-down assays revealed no substantial impact of nuclease treatment on ADR-2 dimerization (Supplementary Fig. S1C). Furthermore, we removed the dsRBD domain of ADR-2, and pull-down assays revealed that the dsRBD deletion did not disrupt the dimerization of ADR-2 (Supplementary Fig. S1G). These data strongly supported the idea that the ADR-2 dimerization is RNA-independent, unlike *Drosophila melanogaster* ADAR dimerization [15].

We developed a mass spectrometry-based method to detect the product inosine, reflecting ADR-2 editing activity (Supplementary Fig. S1H). RNA sequences, comprising 57 bp from intron 6 of the *dyf-5* gene, were synthesized as potential editing substrates for ADR-2 (Supplementary Fig. S1G) [12]. Mass spectrometry analysis revealed that wild-type ADR-2 exhibited editing activity independent of ADBP-1 (Fig. 1C and D). These findings establish the autonomous A-to-I editing activity of dimeric ADR-2 in the absence of ADBP-1, which constitutes a novel mechanism of action [21].

Overall structure of the heterotetrameric ADR-2–ADBP-1 complex

The editing activity of ADR-2 may be regulated by its partner protein ADBP-1 [8] (Fig. 1B), potentially via stabilization of the ADR-2 homodimer. To validate this hypothesis, we transiently coexpressed recombinant ADR-2 and ADBP-1 from HEK293F cells (Supplementary Fig. S2A and B). After pull-down, we performed sequential anion exchange chromatography followed by SEC to obtain the a highly purified ADR-2–ADBP-1 complex in an elution volume of 1.69 ml (Supplementary Fig. S2C and D). Label-free thermal shift experiments demonstrated that the ADR-2–ADBP-1 complex was more stable than the ADR-2 homodimer (Supplementary Fig. S2E). Moreover, ribonuclease treatment revealed that ADR-2 can form a stable complex with ADBP-1 in the absence of RNA (Supplementary Fig. S2F and G).

Next, to solve the structure of the ADR-2–ADBP-1 complex, we collected cryo-EM micrographs of the ADR-2–ADBP-1 complex (Supplementary Fig. S3). After processing the micrographs with cryoSPARC with C1 symmetry, we obtained a map of the ADR-2–ADBP-1 complex at an overall resolution of 3.29 Å (Fig. 1E and F), as determined by gold-standard Fourier shell correlation (FSC) at 0.143 [40], which enabled us to unambiguously build the atomic model of most parts of the ADR-2–ADBP-1 complex (Fig. 1G and Supplementary Fig. S3G). Overall, the ADR-2–ADBP-1 complex adopted a heterotetrameric form with 2:2 stoichiometry (the subunits were designated ADBP-1a, ADBP-1b, ADR-2a, and ADR-2b) and an elongated structure with the approximate dimensions of 127.8 × 98.5 × 83.7 Å (Fig. 1E and G).

ADBP-1 formed a homodimer through its C-terminal region, with the middle region of each ADBP-1 tightly bound to one ADR-2 subunit (Fig. 1G). ADR-2a formed an asymmetric homodimer with ADR-2b, with the catalytic center of

ADR-2b in an open state, but the counterpart site of ADR-2a in a blocked state, reminiscent of hADAR2 [18, 41] (Fig. 1H and I). The editing site of ADR-2a was sterically constrained by two peptide fragments: T377–I389 of ADR-2a and S283–E298 of ADR-2b, resembling two doors keeping the editing site closed (Fig. 1I). As expected, a zinc ion was observed in the conserved pocket of each ADR-2, coordinated by H191, C244, and C305, which plays a critical role in the deaminating process (Fig. 1H and I). Furthermore, near the catalytic site of each ADR-2, an endogenous inositol hexakisphosphate was captured in a large pocket shaped by conserved basic amino acids, including R197, K308, K429, K457, K467, R484, and K485 (Fig. 1J and Supplementary Fig. S3H).

Structural basis for the asymmetric ADR-2 homodimer

Further structural analysis revealed that the interface between the ADR-2 subunits is slightly smaller (∼ 737 Å^2 ; $\triangle G$: −5.6 kcal/mol) than the counterpart interface in the RNA-bound hADAR2 complex (1034 Å^2; $\triangle G$: −2.9 kcal/mol) (PDB ID: 6VFF) but exhibits a lower temperature coefficient (Supplementary Fig. S4A and B) [18]. These differences may be attributable to ADBP-1, which potentially makes homodimeric ADR-2 more compact. The data collectively suggest that ADR-2 forms a homodimer mainly through integrated forces. Of note, a conserved short helix of ADR-2b (amino acids F291–G297) was observed in the interface of the ADR-2 proteins (hereafter referred to as the dimerization helix [18]), which is crucial for the dimerization of ADR-2 via various forces (Fig. 2A). Residues R248, K251, K252, R268, and R386 make the surface of ADR-2a positively charged, which facilitates electrostatic interactions with the negatively charged residues E286, D292, and E298 in ADR-2b (Fig. 2B and C, and Supplementary Fig. S4C). Interestingly, D503, a counterpart of ADR-2 D292, is indispensable for hADAR2 dimerization [18], which supports the role of D292 in ADR-2 dimerization. Moreover, M295 in the dimerization helix of ADR-2b interacts with K251 and K252 on ADR-2a, and M296 of ADR-2b forms a hydrogen bond with S382 of ADR-2a. In addition, an ethyl methane sulfonate (EMS)-induced genetic screening assay demonstrated that a G293R mutation in the dimerization helix and R386Q mutation in the dimerization interface could rectify the ciliary defects related to DYF-5CA (Fig. 2D, and Supplementary Fig. S4D and E), suggesting that G293 and R386 are also essential for ADR-2 editing. Pull-down assay revealed that G293R or R386Q mutation can also impact ADR-2 dimerization (Supplementary Fig. S4F). Therefore, the interface-located amino acids not only play an essential role in the dimerization of ADR-2 but also regulate the editing activity of ADR-2. Amino acid sequence alignment revealed that most residues forming the interface of the ADR-2 homodimer are highly conserved across species (Supplementary Fig. S4G), such that they may provide a general structural basis for the dimerization of ADAR proteins.

The ADBP-1 homodimer extensively interacted with the ADR-2 dimer via a flexible loop

Like ADR-2, ADBP-1 formed a homodimer via its C-terminal residues F177–I214 (Fig. 2E and F). Structural analysis revealed that the C-terminus of ADBP-1 displays a U-shaped structure comprising two short helices, which feature a large proportion of hydrophobic amino acids, including F177, A181, V184, A185, L188, I199, I203, and I207 (Fig. 2G). The strong hydrophobic surface provided an interface for the U-shaped C-terminus to form an auto-crossed homodimer. Further, overexpressing F177A and I203A mutants in *dyf-5CA* did not restore cilia length (Supplementary Fig. S5A), indicating that ADBP-1 dimerization is not essential for ADR-2 function.

ADR-2 interacted with ADBP-1 through a large surface of ∼3200 Å^2 (Supplementary Fig. S5B). Structural analysis demonstrated that integrated hydrophobic effects, electrostatic interactions, and hydrogen bonds form the ADR-2–ADBP-1 complex. ADBP-1 contains three hydrophobic residue-enriched regions, including L77–L90, L107–F136, and L139–K145 (Fig. 2H and Supplementary Fig. S5C), which are stably trapped in the hydrophobic grooves on the surface of ADR-2. We mutated all four loci of ADBP-1 (K137, L139, V141, and K145) to alanine (A) and overexpressed the mutants in *dyf-5CA*, resulting in a failure to restore cilia length (Supplementary Fig. S5A). However, mutations at L77A, I81A, and R87A were associated with cilia recovery (Supplementary Fig. S5A), likely due to the weakened interaction between ADBP-1 and ADR-2 caused by these mutations (Supplementary Fig. S5D). Moreover, in a genetic screen for EMS-induced *dyf-5CA* mutants, we observed that the ADBP-1 mutations P85L and G86S/G86D restored the ciliary defect in *dyf-5CA* (Fig. 2D and Supplementary Table S2). Together, these findings suggest that the fragment encompassing L77–R87 may regulate the editing activity of ADR-2. The residues K145 and E150 from ADBP-1b formed charge interactions with E455, D488, and R487 of ADR-2b; meanwhile, R189, E122, and K145 from ADBP-1a formed charge interactions with D292, K134, E455, and D448 of ADR-2a (Fig. 2I–L). Unlike the dimerization helix of ADR-2b, which stabilized the ADR-2 homodimer, the dimerization helix of ADR-2a (F291–G297) served as a hub by simultaneously interacting with ADR-2b, ADBP-1a, and ADBP-1b (Supplementary Fig. S5E). Hydrogen bonds were formed between R189 of ADBP-1b and G297 of ADR-2a, and between R189 and Q157 of ADBP-1a and D292 and F291 of ADR-2a, respectively. Additionally, M296 and M295 of ADR-2 are positioned within a hydrophobic cluster formed by A181, A182, A185, and V178, which collectively stabilize the dimerization helix (Supplementary Fig. S5E). Collectively, these findings indicate that the unique partner protein ADBP-1 contacts with ADR-2 via integrated forces, including hydrogen bonds, electrostatic interactions, and hydrophobic forces, which reveals a specific regulatory mechanism by which ADBP-1 modulates ADR-2 editing.

RNA substrates recruited to the dsRBD disassociated the ADR-2 dimer

To explore the structural basis for ADR-2 recognition and editing of RNA substrates, we sought to obtain the ADR-2–dsRNA complex by incubating ADR-2 with RNA substrates. Electrophoretic migration gel transfer assays (EMSAs) demonstrated ADR-2 proteins could delay the migration of RNA substrates in the absence of ADBP-1 (Supplementary Fig. S6A); however, the addition of ADBP-1 significantly enhanced the strength of the gel shift pattern and reduced the concentration threshold for ADR-2 binding to RNA (Fig. 3A and Supplementary Fig. S6B), indicating that ADBP-1 may increase the RNA-binding affinity of ADR-2 [42]. Further, we

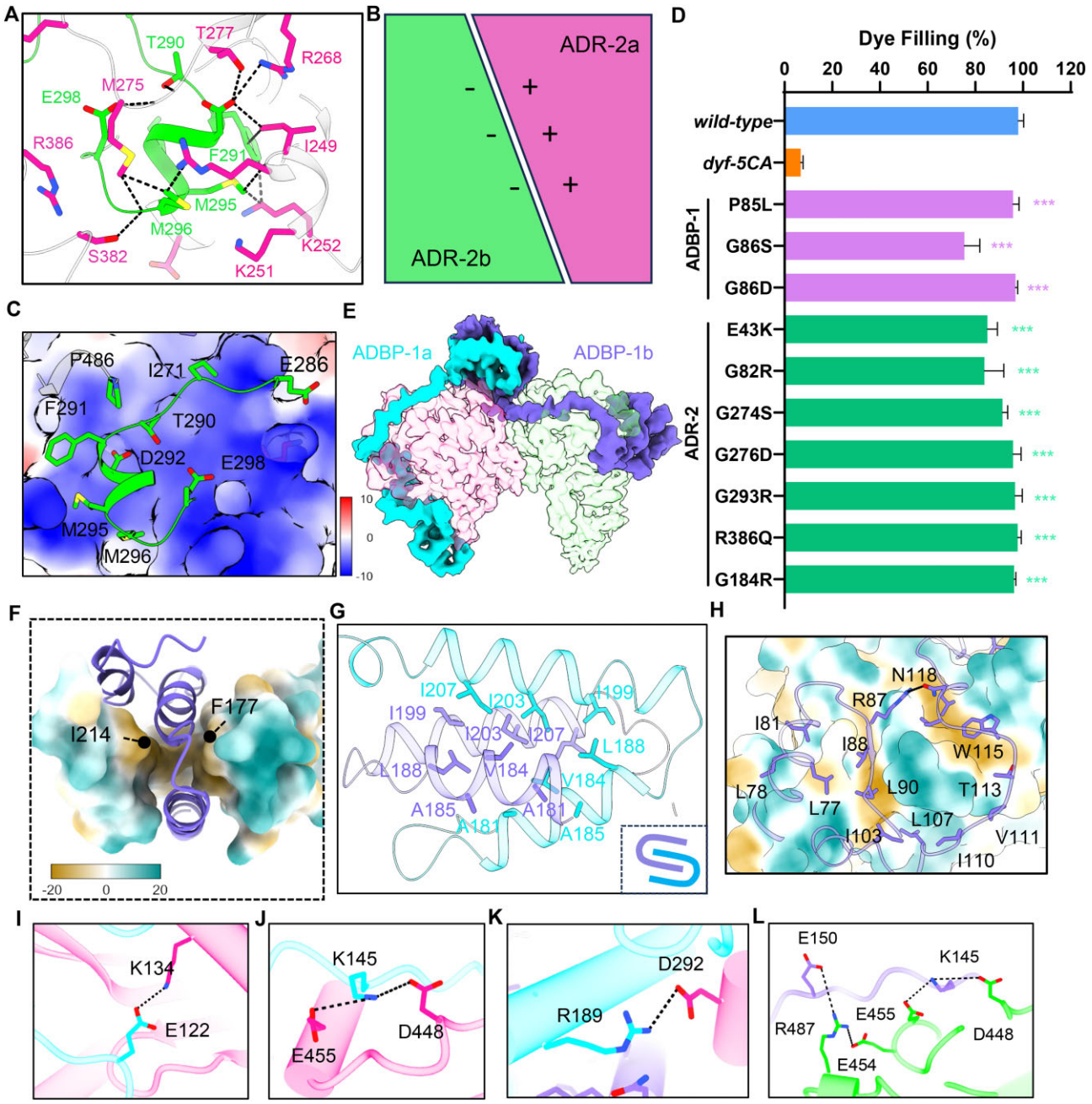

Figure 2. Cryo-EM analysis of ADR-2–ADBP-1 tetramer complex. (**A**) ADR-2 dimers engage in interactions via dimerization helix in ADR-2b. Detailed view of amino acid interactions represented by sticks. (**B**) Schematic representation of the electrostatic potential distribution pattern of ADR-2 monomer at the dimer interaction interface. (**C**) ADR-2a shows a positively charged electrostatic potential surface at the dimer-interacting interface. The charged amino acid residues involved in ADR-2b interactions are represented by sticks. (**D**) EMS-induced mutations in the ADR-2–ADBP-1 complex resulted in a percentage of dye-filling positive animals in the indicated strains (mean ± SD). $N = 100$ to 200, statistical significance, compared to the *dyf-5CA* group, was determined using Student's *t*-test; $***P < 0.001$. (**E**) Cryo-EM density representation of ADBP-1 forming a bowknot-like homodimer in a tetrameric complex. (**F**) Hydrophobicity and hydrophilic interaction analysis of two short helices at the ADBP-1 interface. The 177–214 amino acid segment of ADBP-1 exhibits surface hydrophobicity, while that of ADBP-1b's are shown as cartoons. (**G**) Key hydrophobic amino acid residues interacting at the ADBP-1 homodimer interface. (**H**) ADR-2 binds to hydrophobic fragments (L78–N118) on the ADBP-1 protein via the elongated hydrophobic groove. The ADR-2b exhibits surface hydrophobicity and the interacting amino acids in ADBP-1b are shown as sticks. (**I**–**L**) A close-up view of the salt bridge interactions between ADR-2 and ADBP-1 is presented for ADR-2a and ADBP-1a (I–K), as well as ADR-2b and ADBP-1b (L).The corresponding amino acid residues are also shown as a stick model. Dark dashed lines indicate a salt bridge.

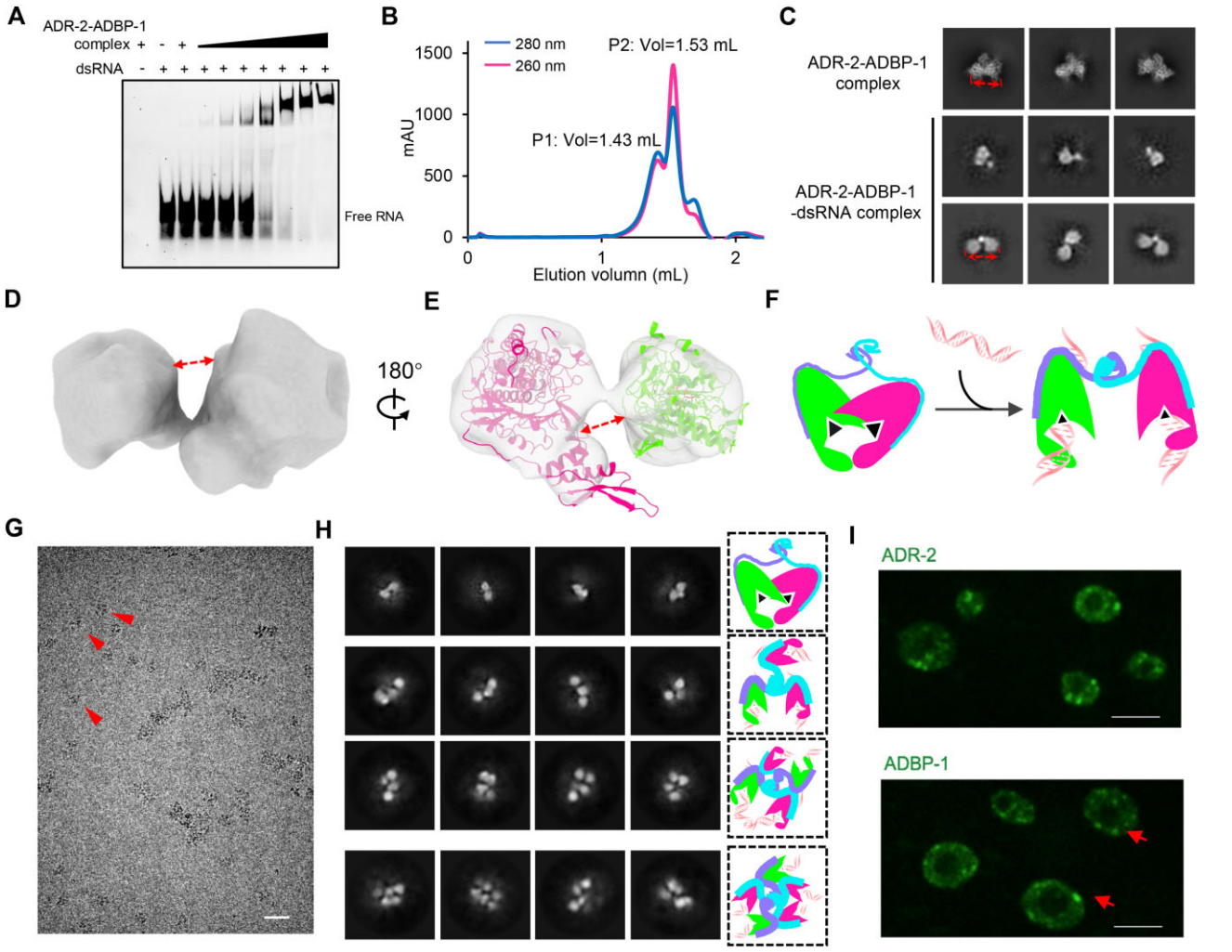

Figure 3. RNA substrates recruited to the dsRBD disassociated the ADR-2 dimer. (**A**) EMSA gel-shift dsRNA binding experiments of ADR-2–ADBP-1 complexes. (**B**) Size exclusion chromatogram of ADR-2–ADBP-1 complex with substrate dsRNA (57 bp). (**C**) Comparison of typical 2D class averages for ADR-2–ADBP-1 complex and ADR-2–ADBP-1–dsRNA complexes. (**D** and **E**) Low-resolution electron density map of reconstructed ADR-2–ADBP-1–dsRBD complex (D) and fitting of ADR-2 monomer atomic models into a 3D density map, respectively (E). Arrows indicate significant movements between ADR-2 monomers. (**F**) Proposed schematic of the ADR-2–ADBP-1 pattern for substrate RNA editing. (**G**) Representative cryo-EM image of Peak1 ADR-2–ADBP-1–dsRNA complexes. Several typical aggregates are marked by arrows. (**H**) Typical 2D class averages of the complex. Typical pattern diagrams for 2D classification are labeled in the box on the right. (**I**) Fluorescence microscopy of *C. elegans* body wall muscle cells that express ADR-2-EGFP (upper) and ADBP-1-EGFP (down); scale bars: 10 μm.

reverse-transcribed the edited dsRNA substrate E5I8 (from exon 5 to intron 8 of the *dyf-5* gene) into DNA and determined the ADR-2 editing sites using sanger sequencing (Supplementary Fig. S1I and S6C). The results indicated that ADBP-1 may enhance ADR-2 editing activity by promoting substrate RNA binding (Supplementary Fig. S6D). Of note, EMSAs and label-free thermal transfer experiments revealed that dsRBD deletion decreased the RNA-binding capacity and stability of the ADR-2–ADBP-1 complex (Supplementary Fig. S6E–G), which is consistent with the observation that the mutations E43K and G82R in the dsRBD rescued the ciliary defects observed in *dyf-5CA* (Fig. 2D, Supplementary Fig. S6H, 6I and Supplementary Table S1). Interestingly, deleting both the dsRBD of ADR-2 and amino acids 1–66 of ADBP-1 did not affect the assembly of the ADR-2–ADBP-1 complex (Supplementary Fig. S6J); however, the RNA-binding capacity was completely lost and reduced editing activity was observed (Supplementary Fig. S6D and F), indicating that dsRBD-mediated RNA binding regulates the editing activity of the ADR-2–dsRNA complex. Together, these findings suggested that, for the whole ADR-2–ADBP-1 complex, the dsRBD is essential for the recruitment of RNA substrates, and a putative role of ADBP-1 is to regulate RNA-binding affinity.

We then assembled the ADR-2–ADBP-1–dsRNA complex by incubating ADR-2–ADBP-1 with RNA substrates (Fig. 3A). Our SEC curves revealed that, compared with the apo ADR-2–ADBP-1 complex (eluted at 1.69 ml), the ADR-2–ADBP-1 complex eluted earlier, with an A280/260 ratio <1.75 and two distinct peaks (Peak 1 and Peak 2) after adding dsRNA substrates (Fig. 3B and Supplementary Fig. S6K). Moreover, the editing assay revealed that both Peak 1 and Peak 2 complexes exhibited editing activity (Supplementary Fig. S7), implying that the ADR-2–ADBP-1–dsRNA complex could adopt multiple organizational models, potentially mediating different biological activities.

Next, we prepared a cryo-EM sample of the ADR-2–ADBP-1–dsRNA complex eluted from Peak 2 due to its symmetric curve (Fig. 3B). Surprisingly, two-dimensional average results revealed that, in contrast to the compact ADR-2 dimer observed in the apo ADR-2–ADBP-1 complex, all ADR-2 proteins adopted monomer or loose dimer conformations with limited structural features (Fig. 3C). This observation was corroborated by the final 3D map, which clearly displayed spatial separation between the ADR-2a and ADR-2b subunits (Fig. 3D and E). Further structural analysis demonstrated that while the ADR-2–ADBP-1 complex maintains a sterically hindered catalytic site within its compact conformation and retains the capability for *in vitro* biochemical reconstitution with dsRNA, the cryo-EM map provides direct evidence for RNA-induced dimer dissociation. Notably, the conformational reorganization of the ADR-2 dimer creates two full functional catalytic sites, thereby potentially increasing RNA editing efficiency (Fig. 3F).

LLPS triggered hyper-editing by the ADR-2–ADBP-1 complex

We also analyzed the organization of the ADR-2–ADBP-1–dsRNA complexes in the SEC Peak 1 fractions (Fig. 3B). Unexpectedly, we observed ADR-2–ADBP-1–dsRNA aggregates in the raw micrographs (Fig. 3G). Subsequent data analysis revealed that ADR-2 proteins not only formed a loose homodimer but also organized into trimers, tetramers, and oligomers (Fig. 3H). Moreover, the proteins eluted from Peak 1 exhibited substantial editing activity (Supplementary Fig. S7), suggesting that the dynamic organization of ADR-2 proteins in the presence of dsRNA may represent a regulatory mechanism of ADR-2 editing under *in vivo* conditions. Fluorescent imaging analysis revealed a punctate distribution pattern of ADR-2 and ADBP-1 (Fig. 3I), indicating the ADR-2–ADBP-1 complex may aggregate under *in vivo* conditions, consistent with the aggregation observed in EM micrographs (Fig. 3H). These data suggest that the ADR-2–ADBP-1 complex may undergo LLPS, which regulates its editing activity.

As expected, both ADR-2 and ADBP-1 have liquid-like characteristics under *in vivo* conditions, as evidenced by spatiotemporal analysis of fluorescence recovery after photobleaching (FRAP), which revealed rapid redistribution of fluorescence from the unbleached to the bleached region (Fig. 4A and B). Next, we investigated the potential LLPS mechanism of the ADR-2–ADBP-1 complex under *in vitro* conditions using an Alexa Fluor™ 488-labeled ADR-2–ADBP-1 complex. We incubated a high concentration of proteins with 4% PEG-8000 to induce LLPS (Fig. 4C and Supplementary Fig. S8A) and found that the ADR-2–ADBP-1 complex undergoes LLPS across a range of concentrations, with diverse condensate size distributions (Supplementary Fig. S8A). Notably, smaller droplets fused upon contact, resulting in the formation of larger droplets (Fig. 4D). Furthermore, our investigation highlighted that *dyf-5* mRNA can augment this phase separation phenomenon (Supplementary Fig. S8B), and FRAP experiments showed that the addition of *dyf-5* RNA to the ADR-2–ADBP-1 complex accelerated the recovery of fluorescence after photobleaching (Fig. 4E and F). However, we found that LLPS of the ADR-2–ADBP-1 complex rarely occurred in the absence of the dsRBD (Supplementary Fig. S8C). These findings led us to speculate that RNA recruitment by the dsRBD plays an essential role in inducing LLPS of the ADR-2–ADBP-1 complex. To study the impact of LLPS on the editing activity of the ADR-2–ADBP-1 complex, we assessed the editing sites on E5I8 under both LLPS and non-LLPS conditions using sanger sequencing. Using a low concentration of the ADR-2–ADBP-1 complex (1 μM), we primarily observed single-base editing events on dsRNA substrates (Fig. 4G–I). However, when the concentration of the ADR-2–ADBP-1 complex was increased to 2.5 or 5 μM, ∼30% of adenine clusters were edited. This percentage increased to 40% under LLPS conditions, which were generated by the addition of PEG (Fig. 4J). Strikingly, deletion of either the ADR-2 dsRBD or the N-terminus (1–66 aa) of ADBP-1 led to a significant decrease in the A-to-I editing activity of the complex (Supplementary Fig. S6D). Moreover, the ADR-2 (△dsRBD)–ADBP-1 complex essentially lost its phase transition ability (Supplementary Fig. S8C). Notably, PEG supplementation did not improve the editing efficiency of this truncated complex (Supplementary Fig. S6D), indicating that the observed enhancement in wild-type complexes is specifically attributable to LLPS-mediated compartmentalization rather than any direct effects of PEG8000. Our findings indicate that phase-separated condensates function as specialized microenvironments that enhance the enzymatic activity of the ADR-2–ADBP-1 complex.

A hypothetical working model for *C. elegans* ADR-2

Previous data showed that ADAR proteins mediate A-to-I editing in certain imperfect dsRNA sequences in a highly specific manner [1, 43]. However, *C. elegans* ADR-2 also performs hyper-A-to-I modification of *dyf-5* dsRNA, displaying non-specific base content priority, which resembles mammalian ADAR editing of the large regular duplexes formed between inverted repeats of long interspersed nucleotide elements in primates or small interspersed nucleotide elements found in mouse [44–46]. This begs the question of how ADAR proteins edit RNA substrates with high efficacy under various conditions. Here, we propose a *C. elegans* ADR-2 editing model based on organizational transitions of the ADR-2–ADBP-1 complex, as observed by electron and light microscopy. ADR-2 and ADBP-1 initially form a stable, compact complex with a stoichiometric ratio of 2:2; in this conformation, one editing site is in an open state and the other is blocked. The overall conformation of the apo ADR-2–ADBP-1 complex is similar to the dsRNA-bound ADR-2 complex (PDB ID: 6VFF) (Supplementary Fig. S9A and B), which led us to believe that the apo ADR-2–ADBP-1 complex may represent a competent state for recruiting and editing certain dsRNA substrates, possibly site-specific substrates. As RNA levels increase, the ADR-2 dimer tends to dissociate, and ADR-2 forms loose dimers, or trimers, tetramers, and multimers with each editing site in a competent state, thereby enabling ADR-2 to catalyze more A-to-I modifications on dsRNA substrates. However, long RNA substrates, such as *dyf-5* RNA, can induce ADR-2 proteins to form highly condensed puncta through LLPS, in which ADR-2 and its RNA substrates aggregate in high concentrations, providing a platform for RNA substrates to be hyper-edited by ADR-2 (Fig. 5). Our working model may explain how ADAR proteins adjust their editing, via conformational changes and LLPS, to achieve different goals under various physiological and pathological conditions.

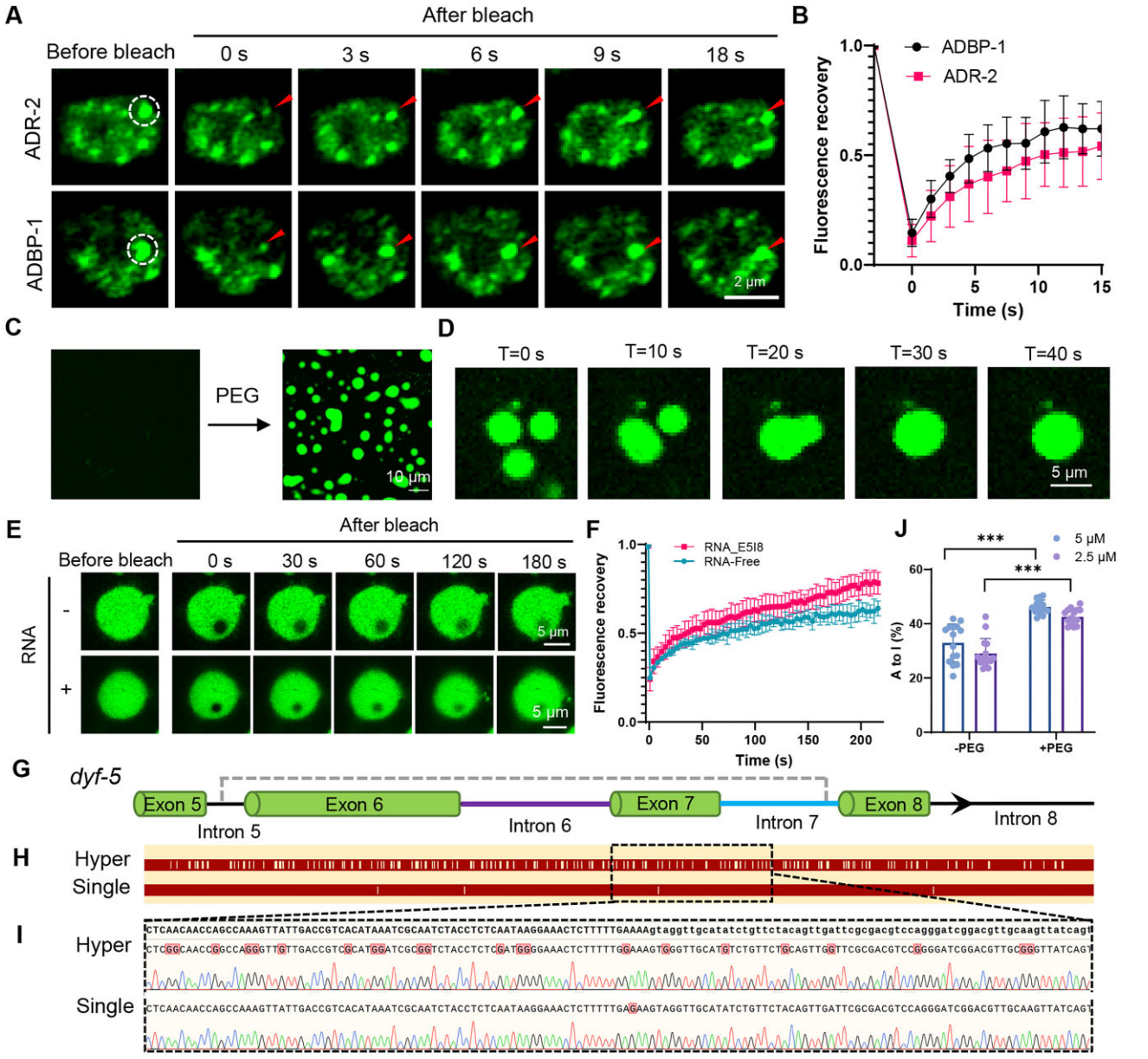

Figure 4. LLPS triggered hyper-editing by the ADR-2–ADBP-1 complex. (**A**) FRAP of ADR-2 (upper) and ADBP-1 (down) condensates *in vivo*, respectively. Time 0 indicates the time of the photobleaching pulse. Scale bar: 5 μm. Data are representative of ten independent experiments. (**B**) Plot showing the time course of the recovery after photobleaching ADR-2–ADBP-1 complex and ADR-2–ADBP-1–dsRNA complex droplets. Data are presented as mean ± SD ($n = 10$). (**C**) *In vitro* phase separation assay of 10 μM ADR-2–ADBP-1–dsRNA complexes in the presence of PEG. Scale bars: 10 μm. Data are representative of five independent experiments. (**D**) Time-lapse micrographs of merging droplets. Data are representative of five independent experiments. (**E**) *In vitro* FRAP analysis of ADR-2–ADBP-1 (upper) and ADR-2–ADBP-1–dsRNA (down) droplets. Time 0 indicates the time of the photobleaching pulse. Scale bar: 5 μm. Data are representative of five independent experiments and data are presented as mean ± SD. (**F**) Plot showing the time course of the recovery after photobleaching ADR-2–ADBP-1 complex and ADR-2–ADBP-1–dsRNA complex droplets. Data are presented as mean ± SD ($n = 5$). (**G**) Schematic diagram illustrates the gene structure of *dyf-5* (exon 5 to intron 8, namely E5I8). (**H**) Distribution pattern of RNA editing sites at the *dyf-5* locus. Vertical lines indicate the positions of the editing sites. (**I**) Illustration of sequencing peak plots for edited loci. The shaded regions on the sequence represent the edited loci. (**J**) Statistical analysis of the number of editing sites in substrate E5I8. The editing activity of the ADR-2–ADBP-1 complex was evaluated both in the presence (+PEG) and absence (−PEG) of PGE8000, at protein concentrations of 5 and 2.5 μM. Statistical analysis was conducted using Student's *t*-test. ***$P < 0.001$. Data are presented as mean ± SD ($n = 15$).

Discussion

Structural differences under different conditions

We prepared cryo-EM specimens of the ADR-2–ADBP-1 complex in a buffer containing Nonidet P-40 [47], which was reported to increase protein stability. This facilitated the creation of a high-resolution EM map of the ADR-2–ADBP-1 complex at 3.29 Å, which revealed two intact dsRBDs in different orientations (Supplementary Fig. S3). This is the first structure of a dimeric ADAR protein that shows two dsRBDs. Notably, the presence of Nonidet P-40 has little effect on ADR-2 editing activity (Supplementary Fig. S7), consistent with the findings of prior studies [48, 49], confirming that it functions to stabilize the dsRBDs to enhance ADAR complex stability. We conducted a structural comparison analysis by aligning the deaminase domains of each ADR-2 in the ADR-2–ADBP-1 complex and found that the deaminase domains vary subtly; the dsRBD of ADR-2b is rotated inward by ~80°

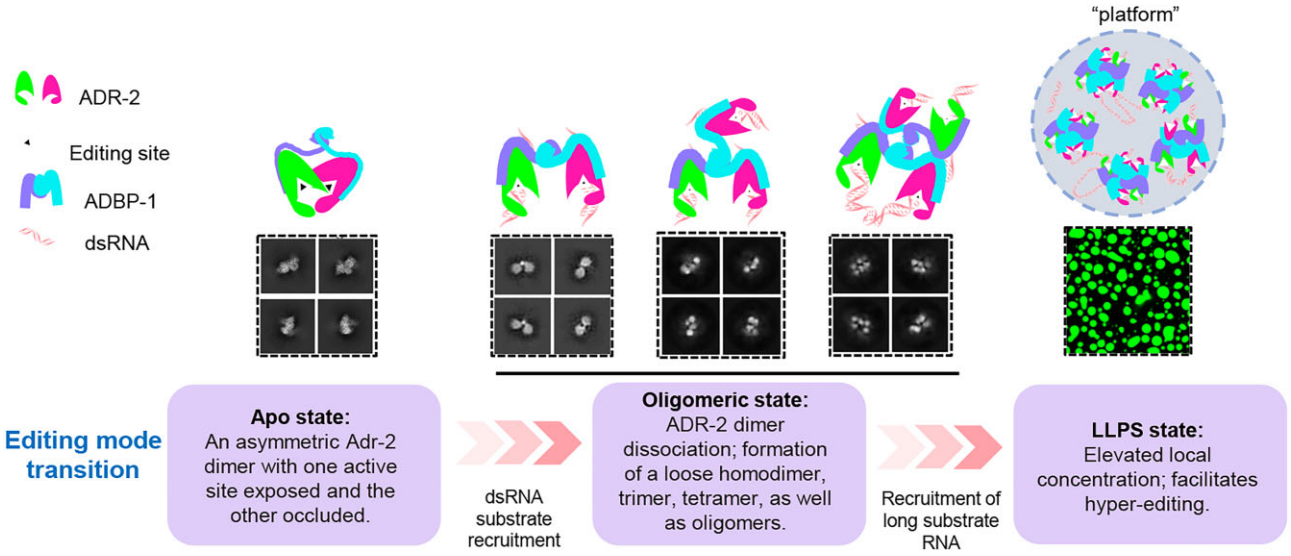

Figure 5. A hypothesized working model of *C. elegant* ADR-2. ADR-2 and ADBP-1 initially form a stable dimer with only one competent editing site. As RNA concentration increases, the ADR-2 dimer will dissociate, forming looser dimer, trimer, tetramer, as well as oligomers and yielding more editing sites for more efficient A-to-I modifications. Long RNA substrates like *dyf-5* RNA induce ADR-2 aggregation through LLPS, enabling hyper RNA editing.

compared with that of ADR-2a (Supplementary Fig. S4H–K). This suggests that the variant dsRBD directions might play a role in adjusting the binding of RNA substrates during the RNA editing process.

Catalytic site comparison between hADAR2 and *C. elegans* ADR-2

During RNA editing, ADAR forms a high-energy intermediate with a tetrahedral center, representing a transient and unstable state [50], which poses considerable challenges in obtaining a high-resolution structure of the dsRNA-bound ADR-2–ADBP-1 complex. Supporting this idea, the reported structure of RNA-bound hADAR2 was obtained by mutating hADAR2 and modifying RNA to simulate intermediates in the deamination reaction [17, 18]. The highly conserved nature of the deaminase domain across various species makes it reasonable to model a dsRNA substrate bound to the ADR-2 deaminase, with reference to the crystalized hADAR2 structures (PDB ID: 5HP2; 6VFF) [17, 19]. Interestingly, comparative analysis revealed an EM density corresponding to the D250–L261 loop in the apo ADR-2–ADBP-1 complex; however, the counterpart of the apo hADAR2-D (only the catalytic deaminase domain of hADAR2) structure was absent (PDB ID: 1Z7Y, corresponding to S458–R474), indicating this loop may be dynamic under certain conditions (Supplementary Fig. S5F–H). Notably, this loop exhibited a parallel position to the dsRNA helix in the hADAR2-D–dsRNA structure (PDB ID: 5HP2), serving as an essential site for fixing the dsRNA substrate; however, the D250–L261 loop in our ADR-2 structure demonstrated a steric clash with the dsRNA substrates (Supplementary Fig. S5H). These findings suggested that the D250–L261 loop may play a crucial, conserved role in coordinating dsRNA substrates with the editing sites of ADAR proteins.

ADR-2 may have a unique base-flipping mechanism

It is worth noting that the conserved residue E488 on the base flip-loop (i.e. amino acids 487–489), which flips the adenosine base for deamination in many ADAR proteins [17], has been replaced by M275 in *C. elegans* ADR-2 (Supplementary Fig. S5G and 5I). Mutations in two glycine residues, G274S or G276D flanking M275, rescued the cilia defect in *dyf-5CA* (Fig. 2D and Supplementary Table S2), further confirming the flip-loop plays an important conserved role in the RNA editing process of ADAR proteins. Moreover, structural comparison revealed that the T381–R386 loop positioned above ADR-2's catalytically active center acts as a door, hindering the base from flipping into the editing site. Therefore, we have designated the T381–R386 loop the "door" (Supplementary Fig. S5J). In contrast, the counterpart door (N589–A595) in hADAR2-D is in an open state, allowing ample space for the base to flip (Supplementary Fig. S5J). However, this door loop sequence is poorly conserved (Supplementary Fig. S3E), suggesting the existence of distinct base-flipping regulatory mechanisms among ADAR proteins.

The potential roles of ADBP-1

The poor cryo-EM density of the N-terminus of ADBP-1 (amino acids 1–66) is likely due to its intrinsic flexibility, as predicted by Alphafold (structure ID: AF-G5EDW1-F1 [51, 52]) (Supplementary Fig. S9C). Surface charge analysis revealed many positively charged residues at the N-terminus of ADBP-1 (Supplementary Fig. S9D). Moreover, the N-terminal region is spatially adjacent to the dsRBD of ADR-2, and the presence of ADBP-1 could increase ADR-2 RNA-binding affinity. Additionally, the predicted structure of the ADR-2–ADBP-1 complex demonstrates that the 1–66 amino acid region of ADBP-1 may regulate the dsRBD of ADR-2 (Supplementary Fig. S9E). Collectively, we hypothesize that the N-terminus of ADBP-1 may influence substrate RNA binding activity by regulating the dsRBD of ADR-2 (Supplementary Fig. S9F). In *C. elegans*, although it lacks a nuclear localization signal, ADR-2 can locate to both the nucleus and cytoplasm. Its nuclear localization relies on ADBP-1, indicating that ADBP-1 may restrict the editing events of the ADR-2–ADBP-1 complex to the nucleus. As ADR-2 can local-

ize to the cytoplasm and form a homodimer with editing activity in the absence of ADBP-1, we speculate that nuclear and cytoplasmic ADR-2 may possess different editing functionalities characterized by distinct substrate selection and capacity.

In summary, we used cryo-EM and light microscopy, in combination with editing assays, to observe how organizational rearrangements of the ADR-2 and ADR-2–ADBP-1 complexes alter the editing mode of ADR-2, from minimal editing with a blocked catalytic site in the ADR-2 dimer to hyper-editing facilitated by numerous competent catalytic sites in LLPS-mediated ADR-2 puncta. These findings provide new insights into the working mechanisms of ADAR proteins, provide a structural explanation for ADAR-mediated hyper-editing of RNA substrates, and offer insights into the development of more efficacious RNA editing tools.

Acknowledgements

We thank all staffs at the Cryo-EM Center of Southern University of Science and Technology and Chunlong Guo, Zhenqian Guo, Chuan Liu, Fanhao Meng, Li, and other staff members at Shuimu BioSciences Ltd. for their assistance in data collection. Z.L. is an investigator of SUSTech Institute for Biological Electron Microscopy. We thank Chen Zhe for assistance with the dye-filling assay and data analysis.

Author contributions: Z.L. and G.O. conceived and designed the project. J.M., X.L., and Z.Z. prepared and purified the proteins. J.M. and X.L. prepared the cryo-EM specimens. J.M. and C.X. collected the EM data. J.M. and C.W. performed the cryo-EM analysis and the model building. J.M., Y.F., and X.C. analyzed LLPS *in vitro*. J.M., J.Y., and Y.C. performed the LC/MS assay. Y.F. analyzed the sanger sequence. K.X. and Z.W. performed the analysis of LLPS *in vivo* and conducted the dye-filling assay. J.M., G.O. and Z.L. drafted the manuscript.

Supplementary data

Supplementary data is available at NAR online.

Conflict of interest

None declared.

Funding

This work was supported by funds from the National Science Foundation of China (Grants 32371275 to Z.L.; 32430026, 31991191, 92254306, and 32021002 to G.O.), Guangdong Basic and Applied Basic Research Foundation (No. 2024A1515011538 to Z.L.), Shenzhen Municipal Basic Research projects (No. JCYJ20210324105007020 to Z.L), Guangdong Innovative and Entrepreneurial Research Team Program (No. 2021ZT09Y104), the Pearl River Talent Recruitment Program (No. 2021QN02Y449 to Z.L), Shenzhen Science and Technology Program (No. ZDSYS20220402111000001), and the start-up funds of Southern University of Science and Technology to Z.L. Funding to pay the Open Access publication charges for this article was provided by the National Science Foundation of China [32371275].

Data availability

The data that support this study are available from the corresponding authors upon reasonable request. The cryo-EM maps and the coordinates have been deposited in the Electron Microscopy Data Bank (EMDB) and Protein Data Bank (PDB) following accession codes: EMD-60042 and 8ZEP for ADR-2-ADBP-1 complex. Source data are provided with this paper.

References

1. Gott JM, Emeson RB. Functions and mechanisms of RNA editing. *Annu Rev Genet* 2000;**34**:499–531. https://doi.org/10.1146/annurev.genet.34.1.499
2. Yang Y, Okada S, Sakurai M. Adenosine-to-inosine RNA editing in neurological development and disease. *RNA Biol* 2021;**18**:999–1013. https://doi.org/10.1080/15476286.2020.1867797
3. Yuan J, Xu L, Bao HJ *et al.* Biological roles of A-to-I editing: implications in innate immunity, cell death, and cancer immunotherapy. *J Experiment Clin Cancer Res* 2023;**42**:149.
4. Eisenberg E, Levanon EY. A-to-I RNA editing—immune protector and transcriptome diversifier. *Nat Rev Genet* 2018;**19**:473–90. https://doi.org/10.1038/s41576-018-0006-1
5. Nishikura K. A-to-I editing of coding and non-coding RNAs by ADARs. *Nature reviews. Mol Cell Biol* 2016;**17**:83–96.
6. Duan Y, Tang X, Lu J. Evolutionary driving forces of A-to-I editing in metazoans. *WIREs RNA* 2022;**13**:e1666. https://doi.org/10.1002/wrna.1666
7. Ganem NS, Ben-Asher N, Manning AC *et al.* Disruption in A-to-I editing levels affects *C. elegans* development more than a complete lack of editing. *Cell Rep* 2019;**27**:1244–53. https://doi.org/10.1016/j.celrep.2019.03.095
8. Tonkin LA, Saccomanno L, Morse DP *et al.* RNA editing by ADARs is important for normal behavior in *Caenorhabditis elegans*. *EMBO J* 2002;**21**:6025–35. https://doi.org/10.1093/emboj/cdf607
9. Goldstein B, Agranat-Tamir L, Light D *et al.* A-to-I RNA editing promotes developmental stage-specific gene and lncRNA expression. *Genome Res* 2017;**27**:462–70. https://doi.org/10.1101/gr.211169.116
10. Samuel CE. ADARs: viruses and innate immunity. *Curr Top Microbiol Immunol* 2012;**353**:163–95.
11. Dhakal A, Salim C, Skelly M *et al.* ADARs regulate cuticle collagen expression and promote survival to pathogen infection. *BMC Biol* 2024;**22**:37. https://doi.org/10.1186/s12915-024-01840-1
12. Li D, Liu Y, Yi P *et al.* RNA editing restricts hyperactive ciliary kinases. *Science* 2021); **373**:984–91. https://doi.org/10.1126/science.abd8971
13. Hedgecock EM, Culotti JG, Thomson JN *et al.* Axonal guidance mutants of *Caenorhabditis elegans* identified by filling sensory neurons with fluorescein dyes. *Dev Biol* 1985;**111**:158–70. https://doi.org/10.1016/0012-1606(85)90443-9
14. Ota H, Sakurai M, Gupta R *et al.* ADAR1 forms a complex with Dicer to promote microRNA processing and RNA-induced gene silencing. *Cell* 2013;**153**:575–89. https://doi.org/10.1016/j.cell.2013.03.024
15. Gallo A, Keegan LP, Ring GM *et al.* An ADAR that edits transcripts encoding ion channel subunits functions as a dimer. *EMBO J* 2003;**22**:3421–30. https://doi.org/10.1093/emboj/cdg327
16. Mboukou A, Rajendra V, Messmer S *et al.* Dimerization of ADAR1 modulates site-specificity of RNA editing. *Nat Commun* 2024;**15**:10051. https://doi.org/10.1038/s41467-024-53777-2
17. Matthews MM, Thomas JM, Zheng Y *et al.* Structures of human ADAR2 bound to dsRNA reveal base-flipping mechanism and basis for site selectivity. *Nat Struct Mol Biol* 2016;**23**:426–33. https://doi.org/10.1038/nsmb.3203

18. Thuy-Boun AS, Thomas JM, Grajo HL *et al.* Asymmetric dimerization of adenosine deaminase acting on RNA facilitates substrate recognition. *Nucleic Acids Res* 2020;**48**:7958–72. https://doi.org/10.1093/nar/gkaa532
19. Macbeth MR, Schubert HL, Vandemark AP *et al.* Inositol hexakisphosphate is bound in the ADAR2 core and required for RNA editing. *Science* 2005;**309**:1534–9. https://doi.org/10.1126/science.1113150
20. Wilkins C, Dishongh R, Moore SC *et al.* RNA interference is an antiviral defence mechanism in *Caenorhabditis elegans*. *Nature* 2005;**436**:1044–7. https://doi.org/10.1038/nature03957
21. Ohta H, Fujiwara M, Ohshima Y *et al.* ADBP-1 regulates an ADAR RNA-editing enzyme to antagonize RNA-interference-mediated gene silencing in *Caenorhabditis elegans*. *Genetics* 2008;**180**:785–96. https://doi.org/10.1534/genetics.108.093310
22. Eliad B, Schneider N, Ben-Naim Zgayer O *et al.* ADBP-1 regulates ADR-2 nuclear localization to control editing substrate selection. *Nucleic Acids Res* 2024;**52**:9501–18. https://doi.org/10.1093/nar/gkae641
23. Yang W, Wang Q, Howell KL *et al.* ADAR1 RNA deaminase limits short interfering RNA efficacy in mammalian cells. *J Biol Chem* 2005;**280**:3946–53. https://doi.org/10.1074/jbc.M407876200
24. Scadden AD, Smith CW. Specific cleavage of hyper-edited dsRNAs. *EMBO J* 2001;**20**:4243–52. https://doi.org/10.1093/emboj/20.15.4243
25. Wolozin B, Ivanov P. Stress granules and neurodegeneration. *Nat Rev Neurosci* 2019;**20**:649–66. https://doi.org/10.1038/s41583-019-0222-5
26. Yang P, Mathieu C, Kolaitis RM *et al.* G3BP1 is a tunable switch that triggers phase separation to assemble stress granules. *Cell* 2020;**181**:325–45. https://doi.org/10.1016/j.cell.2020.03.046
27. Yasuda S, Tsuchiya H, Kaiho A *et al.* Stress- and ubiquitylation-dependent phase separation of the proteasome. *Nature* 2020;**578**:296–300. https://doi.org/10.1038/s41586-020-1982-9
28. Corbet GA, Burke JM, Parker R. ADAR1 limits stress granule formation through both translation-dependent and translation-independent mechanisms. *J Cell Sci* 2021;**134**:jcs259400. https://doi.org/10.1242/jcs.258783
29. Behm M, Wahlstedt H, Widmark A *et al.* Accumulation of nuclear ADAR2 regulates adenosine-to-inosine RNA editing during neuronal development. *J Cell Sci* 2017;**130**:745–53. https://doi.org/10.1242/jcs.200055
30. Lafontaine DLJ, Riback JA, Bascetin R *et al.* The nucleolus as a multiphase liquid condensate. *Nat Rev Mol Cell Biol* 2021;**22**:165–82. https://doi.org/10.1038/s41580-020-0272-6
31. Bhat P, Chow A, Emert B *et al.* Genome organization around nuclear speckles drives mRNA splicing efficiency. *Nature* 2024;**629**:1165–73. https://doi.org/10.1038/s41586-024-07429-6
32. Punjani A, Rubinstein JL, Fleet DJ *et al.* cryoSPARC: algorithms for rapid unsupervised cryo-EM structure determination. *Nat Methods* 2017;**14**:290–6. https://doi.org/10.1038/nmeth.4169
33. Bepler T, Morin A, Rapp M *et al.* Positive-unlabeled convolutional neural networks for particle picking in cryo-electron micrographs. *Nat Methods* 2019;**16**:1153–60. https://doi.org/10.1038/s41592-019-0575-8
34. Pettersen EF, Goddard TD, Huang CRC *et al.* UCSF ChimeraX: Structure visualization for researchers, educators, and developers. *Protein Sci* 2021;**30**:70–82. https://doi.org/10.1002/pro.3943
35. Emsley P, Lohkamp B, Scott WG *et al.* Features and development of Coot. *Acta Crystallogr D Biol Crystallogr* 2010;**66**:486–501. https://doi.org/10.1107/S0907444910007493
36. Afonine PV, Poon BK, Read RJ *et al.* Real-space refinement in PHENIX for cryo-EM and crystallography. *Acta Crystallogr D Struct Biol* 2018;**74**:531–44. https://doi.org/10.1107/S2059798318006551
37. Mahmood T, Yang PC. Western blot: technique, theory, and trouble shooting. *North Am J Med Sci* 2012;**4**:429–34.
38. Perkins LA, Hedgecock EM, Thomson JN *et al.* Mutant sensory cilia in the nematode *Caenorhabditis elegans*. *Dev Biol* 1986;**117**:456–87. https://doi.org/10.1016/0012-1606(86)90314-3
39. Starich TA, Herman RK, Kari CK *et al.* Mutations affecting the chemosensory neurons of *Caenorhabditis elegans*. *Genetics* 1995;**139**:171–88. https://doi.org/10.1093/genetics/139.1.171
40. Rosenthal PB, Henderson R. Optimal determination of particle orientation, absolute hand, and contrast loss in single-particle electron cryomicroscopy. *J Mol Biol* 2003;**333**:721–45. https://doi.org/10.1016/j.jmb.2003.07.013
41. Tian B, Bevilacqua PC, Diegelman-Parente A *et al.* The double-stranded-RNA-binding motif: interference and much more. *Nat Rev Mol Cell Biol* 2004;**5**:1013–23. https://doi.org/10.1038/nrm1528
42. Rajendren S, Manning AC, Al-Awadi H *et al.* A protein–protein interaction underlies the molecular basis for substrate recognition by an adenosine-to-inosine RNA-editing enzyme. *Nucleic Acids Res* 2018;**46**:9647–59. https://doi.org/10.1093/nar/gky800
43. Bass BL. RNA editing by adenosine deaminases that act on RNA. *Annu Rev Biochem* 2002;**71**:817–46. https://doi.org/10.1146/annurev.biochem.71.110601.135501
44. Athanasiadis A, Rich A, Maas S. Widespread A-to-I RNA editing of Alu-containing mRNAs in the human transcriptome. *PLoS Biol* 2004;**2**:e391. https://doi.org/10.1371/journal.pbio.0020391
45. Osenberg S, Paz Yaacov N, Safran M *et al.* Alu sequences in undifferentiated human embryonic stem cells display high levels of A-to-I RNA editing. *PLoS One* 2010;**5**:e11173. https://doi.org/10.1371/journal.pone.0011173
46. Levanon EY, Eisenberg E, Yelin R *et al.* Systematic identification of abundant A-to-I editing sites in the human transcriptome. *Nat Biotechnol* 2004;**22**:1001–5. https://doi.org/10.1038/nbt996
47. O'Connell MA, Keller W. Purification and properties of double-stranded RNA-specific adenosine deaminase from calf thymus. *Proc Natl Acad Sci USA* 1994;**91**:10596–600. https://doi.org/10.1073/pnas.91.22.10596
48. Bass BL, Weintraub H. An unwinding activity that covalently modifies its double-stranded RNA substrate. *Cell* 1988;**55**:1089–98. https://doi.org/10.1016/0092-8674(88)90253-X
49. Kim U, Garner TL, Sanford T *et al.* Purification and characterization of double-stranded RNA adenosine deaminase from bovine nuclear extracts. *J Biol Chem* 1994;**269**:13480–9. https://doi.org/10.1016/S0021-9258(17)36857-6
50. Goodman RA, Macbeth MR, Beal PA. ADAR proteins: structure and catalytic mechanism. *Curr Top Microbiol Immunol* 2012;**353**:1–33.
51. Varadi M, Anyango S, Deshpande M *et al.* AlphaFold Protein Structure Database: massively expanding the structural coverage of protein-sequence space with high-accuracy models. *Nucleic Acids Res* 2022;**50**:D439–44. https://doi.org/10.1093/nar/gkab1061
52. Jumper J, Evans R, Pritzel A *et al.* Highly accurate protein structure prediction with AlphaFold. *Nature* 2021;**596**:583–9. https://doi.org/10.1038/s41586-021-03819-2

Received: August 5, 2024. **Revised:** February 6, 2025. **Editorial Decision:** February 11, 2025. **Accepted:** February 17, 2025